PAPER

Check for updates

Direct synthesis of organic salt-derived porous carbons for enhanced CO_2 and methane storage†

Ibtisam Alali[ab] and Robert Mokaya [ID] *[a]

The direct carbonisation of a carbon-rich organic salt, potassium phthalimide (PPI), generates porous carbons with porosity suitable for energy-related gas storage applications. The PPI-derived carbons exhibit high surface area of up to 2889 m^2 g^{-1} and pore volume of up to 1.36 cm^3 g^{-1}, and the porosity can be readily tailored by choice of the carbonisation temperature and, to a lesser extent, carbonisation time. Depending on the preparation conditions, the PPI-derived carbons can be tailored to have ideal porosity for CO_2 uptake at low pressure, which at 25 °C reaches 1.7 mmol g^{-1} and 5.2 mmol g^{-1} at 0.15 bar and 1 bar, respectively. The carbons also exhibit very impressive methane storage capacities of up to 18.2 mmol g^{-1} at 25 °C and 100 bar. An important finding is that the carbons may be readily compacted to a high packing density of up to 1.10 g cm^{-3} with retention of their textural properties. The consequence of the high packing density of the PPI-derived carbons, coupled with their high gravimetric methane uptake, is that they achieve exceptionally high volumetric uptake of up to 338 cm^3 (STP) cm^{-3} at 25 °C and 100 bar, and volumetric working capacity (100−5 bar pressure swing) of 249 cm^3 (STP) cm^{-3}, which are significantly higher than most porous carbons and metal–organic frameworks (MOFs). PPI is thus a very attractive precursor for the simple synthesis of porous carbons with an unrivalled mix of properties for CO_2 and methane storage applications.

1 Introduction

The demand for crude oil has steadily increased with growth in the world economy, raising concerns over the sustainability of oil reserves and about the associated environmental consequences of continued use of fossil fuels. The emissions of CO_2 from the combustion of fossil fuels are a key global environmental concern. Significant ongoing research efforts are currently focused on finding improved methods for the capture of CO_2 from fossil fuel power stations. However, the capture of CO_2 can only be part of a larger suite of approaches. Of particular interest are efforts aimed at developing alternative cleaner fuels to relieve the environmental pressures and minimise the considerable dependence on crude oil.[1–4] To this end, natural gas and biogas have been touted as ecologically friendly alternative fuels because they are more environmentally benign compared to oil-based fuels; despite the fact that natural gas and biogas still produce CO_2, they burn more cleanly than

conventional liquid or solid hydrocarbon fuels. However, methane, which is the main ingredient of natural gas and biogas, suffers from a low volumetric energy density. Therefore, the use of methane in a variety of applications, particularly for vehicular on-board scenarios, is severely limited. Compression (compressed natural gas, CNG) or liquefaction (liquefied natural gas, LNG) can enhance the volumetric energy density of natural gas, but both of these techniques are expensive and unsuitable for light-duty passenger cars.[1–3] The promising alternative to LNG and CNG is storing methane as an adsorbed phase (adsorbed natural gas, ANG) in porous materials at room temperature and moderate pressure. Reduction in the working pressure would make tanks lighter, smaller and minimise the price and space requirements for the vehicular use of natural gas.[3–5]

The effectiveness or viability of ANG technology depends mainly on improvements in methane storage. Many porous materials have been extensively examined and assessed for methane storage. Early efforts mainly concentrated on zeolites; however, their low surface area, which is typically <1000 m^2 g^{-1}, limits the methane uptake capacity.[3] Metal–organic frameworks (MOFs) have been identified as excellent candidates to meet methane storage needs but suffer from an inability to be compacted without loss of form and porosity meaning that they have low packing density and low volumetric uptake.[6,7] On the other hand, porous carbons are one of the most extensively investigated class of materials for ANG technology, and the

aSchool of Chemistry, University of Nottingham, University Park, Nottingham NG7 2RD, UK. E-mail: r.mokaya@nottingham.ac.uk

bDepartment of Chemistry, College of Science, Jouf University, P. O. Box 2014, Sakaka, Saudi Arabia

† Electronic supplementary information (ESI) available: Eight additional figures; XRD patterns, high resolution XPS spectra, SEM images, isosteric heat of adsorption (Q_{st}) and selectivity plots for CO_2, pore size distribution curves, and comparative volumetric methane uptake isotherms, and five tables; comparative CO_2 and methane uptake. See DOI: https://doi.org/10.1039/d3ta00044c

6952 | *J. Mater. Chem. A*, 2023, 11, 6952–6965

This journal is © The Royal Society of Chemistry 2023

variety of methods for their preparation has resulted in a wide range of porous carbon types.[8,9] One of the most common methods for generating highly porous carbons is chemical activation, which involves heat treatment of carbon precursors impregnated with a chemical activating agent, usually KOH, under an inert atmosphere.[10] However, chemical activation with KOH has some drawbacks, namely, (i) the activating agent is often corrosive and requires special equipment, and (ii) a strict acid washing of the resulting activated carbon is needed to leach out inorganic salts and residual products of activation to release the carbon's porosity.[10] Thus, alternative and simpler methods for preparing highly porous carbons are desirable. Recent reports have proposed using organic salts as precursors for porous carbons. The one-step preparation of porous carbons by carbonising solid organic salts has been achieved from potassium hydrogen phthalate,[11] and other organic salts.[12–14] Carbon aerogels may also be formed using metal salts as template.[15] The metal in the organic salt acts as a porogen, generating porosity upon carbonisation and/or removal. In the case of organic salts, the integral metal can act as an activating agent, allowing porous carbons to be produced directly upon carbonisation, provided the metal is chosen appropriately.[16] This scenario simulates the carbon activation process except that the activating agent and carbon precursor are both provided by the organic metal salt.[11]

Both potassium hydrogen phthalate (KHP) and potassium phthalimide (PPI) have previously been utilised as precursors for porous carbons.[11,17] We have shown that KHP-derived carbons are highly microporous with moderate surface area, which translated to excellent CO_2 uptake at low pressure.[11] However, there appeared to be a limit to the porosity achievable by KHP-derived carbons that topped off at surface area of 2100 $m^2 g^{-1}$ and pore volume of 1.1 $cm^3 g^{-1}$.[11] This means that the porosity of the KHP-derived carbons was suitable for CO_2 uptake at low pressure, but not for CH_4 uptake, which requires higher porosity.[11] PPI-derived carbons, which achieved similar levels of porosity (i.e., maximum surface area and pore volume of 2053 $m^2 g^{-1}$ and 1.14 $cm^3 g^{-1}$, respectively) to that of KHP-derived carbons, have recently been reported.[17] However, their preparation[17] included washing of the carbons in acid after the carbonisation step as opposed to simpler wash with water as demonstrated for KHP-derived carbons.[11] These previous studies on KHP-derived and PPI-derived carbons present two unanswered questions, namely, (i) can these organic salts generate carbons with higher porosity (i.e., surface area > 2100 $m^2 g^{-1}$, and pore volume > 1.1 $cm^3 g^{-1}$) that may be more suited for methane storage, and (ii) can the preparation of PPI-derived carbons be simplified to carbonisation and washing with water rather than acid. In the quest to answer these questions, it is important to note that the presence of N in a precursor has been shown to increase susceptibility to activation and a tendency to generate higher porosity.[18–22] In this regard, polypyrrole (PPY) is known to generate activated carbons with very high porosity.[18–22] Indeed, the porosity of KOH activated carbons can be modulated by judicious addition of PPY to other precursors, wherein the level of porosity trends with the amount of PPY added.[23,24] This suggests that the presence of N in precursors can act as an

in situ porogen. The expectation, therefore, is that the presence of N in PPI means that it should be possible, given the right synthesis procedure, to generate porous carbons with higher porosity than is possible for KHP-derived carbons.

We, therefore, in this work sought to demonstrate the successful preparation of PPI-derived carbons using a simpler method that omits the use of acid washing post carbonisation and which also results in much greater porosity than previously reported for organic salt derived carbons. This expands the range of achievable porosity via carbonisation of PPI, with the consequence that the textural properties can be readily tailored and optimised for exceptional performance in CO_2 capture and storage and/or methane storage.

2 Experimental section

2.1 Porous carbon synthesis

2 g of potassium phthalimide (PPI) was placed in a tubular furnace and heated at a ramp rate of 10 °C min^{-1} to temperatures ranging from 600 to 1000 °C under a flow of nitrogen gas, and held at the final temperature for 2 h. The resulting carbonaceous matter was washed with deionised water and dried at 100 °C. The carbons were denoted as PPI-T-y, where T is the carbonisation temperature (°C), and y is the holding time (h). Two other sets of PPI-derived carbons were similarly prepared at carbonisation temperature of 700 or 800 °C, but by holding at the target temperature for 1, 2, 3 or 4 h. Following washing and drying as described above, the final carbons were designated as PPI-700-y or PPI-800-y, for carbonisation at 700 °C and 800 °C, respectively.

2.2 Material characterisation

Elemental, CHN, analysis was performed on an Exeter Analytical CE-440 Elemental Analyser. A PANalytical X'Pert PRO diffractometer was used to perform powder XRD analysis using a Cu-Kα source (40 kV, 40 mA) with step size of 0.02° and 50 s time step. Nitrogen sorption analysis (at −196 °C) with a Micromeritics 3FLEX sorptometer was used to determine the textural properties. Prior to analysis the carbons were degassed at 200 °C for 16 h under vacuum. The surface area was calculated using the Brunauer–Emmett–Teller (BET) method applied to adsorption data in the appropriate relative pressure (P/P_o) range. The P/P_o range for the determination of surface area was selected to ensure that there was a positive y-axis intercept from multipoint BET fitting (i.e., C > 0) and also that $V_{ads}(1 - P/P_o)$ would rise with P/P_o.[25] The pore volume was estimated from the total nitrogen uptake at close to saturation pressure ($P/P_o \approx$ 0.99). The micropore surface area and micropore volume were determined via t-plot analysis. The pore size distribution (PSD) was determined using non-local density functional theory (NLDFT) applied to nitrogen adsorption data. For PSD determination, SAIEUS software along with the 2D-NLDFT heterogeneous surface kernel was used. This allowed the determinations to adequately take account of the chemical and energetic heterogeneity of the carbons. The fitting parameter, λ, which was between 2.5 and 5.0 within the SAIEUS software,

This journal is © The Royal Society of Chemistry 2023

J. Mater. Chem. A, 2023, 11, 6952–6965 | **6953**

controlled the roughness of the PSD in order to yield realistic PSDs for the carbons. Scanning electron microscopy (SEM) images were recorded using an FEI Quanta 200 microscope, operating at a 5 kV accelerating voltage. To obtain Raman spectra, a Horiba-Jobin-Yvon LabRAM Raman microscope was used with a 532 nm laser operating at *ca.* 4 mW (10%) and a 600 lines per mm grating. The spectra were collected by averaging 8 acquisitions of 60 s duration, and the Raman shift was calibrated with reference to the Rayleigh peak and the 520.7 cm^{-1} Si line from a Si (100) sample. A Kratos AXIS ULTRA was used for X-ray photoelectron spectroscopy (XPS) analysis. A monochromated A1 K X-ray source (1486.6 eV) was used at 10 mA emission current and 12 kV anode potential. A charge neutralizer filament was utilised in order to avoid surface charging, and the analysis chamber pressure was kept at better than 5×10^{-9} Torr. Three distinct areas were analysed for each sample. The binding energies of the spectra were calibrated by setting C-1s to 284.6 eV.

The packing density of the carbons was determined by pressing a known mass of carbon at a compaction pressure of 370 MPa in a 1.3 cm diameter die for 5 minutes at ambient temperature. The packing density could then be worked out from the mass and volume of the resulting carbon pellet.

2.3 Gas uptake measurements

CO_2 uptake was determined in the pressure range 0–20 bar at room temperature using a Hiden Isochema Intelligent Gravimetric Analyser (IGA-003). The carbons were outgassed at 240 °C for several hours prior to performing the CO_2 uptake measurements. Methane uptake was determined using a Hiden Isochema XEMIS Analyser. Before the uptake measurements, the carbon samples were degassed at 240 °C under vacuum for several hours. Methane uptake isotherms were obtained at 25 °C, over the pressure range of 0–100 bar. The experimental gas uptake isotherms were fit to a Toth model using pyGAPS modelling module in order to estimate the isosteric heat of adsorption (Q_{st}). The Q_{st} was calculated according to the Whittaker method using parameters (*i.e.*, n_m, K, m) obtained from the modelling.

3 Results and discussion

3.1 Elemental composition and nature of PPI-derived carbons

The elemental composition of the PPI-derived carbons, *i.e.*, after carbonisation of the PPI, washing with deionised water and drying, is shown in Table 1. We firstly note that the composition of PPI is in line with expectations from the structural formulae. It is interesting to note that the O/C ratio of PPI is relatively low at 0.26. For conventional activated carbons wherein an activating agent is used, precursors with low O/C ratio are known to generate microporous carbons.[23,24,26] However, the presence of N may act to mitigate the trend to micropores.[18–22] As shown in Table 1, the C content rises from 51.3 wt% for PPI to between 73 and 93 wt% for PPI-derived carbons, with the increase being more significant at higher

carbonisation temperature. The N content decreases at higher carbonisation temperature, but all samples still retain some N, which is unusual for potentially highly porous carbons prepared *via* an activation route.[26–30] The nominal O content is low compared to that of activated carbons especially for samples prepared at 800 °C and above.[2–22,26–30] The consequence of this is that at carbonisation temperature of 800 °C and above, the PPI-derived carbons may be considered as being comparatively C-rich (and O-poor) resulting in lower O/C ratio than for KHP-derived carbons and conventional activated carbons in general.[11,22–24,26–30] The carbonisation yield (*i.e.* mass of PPI-derived carbon compared to PPI) is given in Table 1. The overall yield varies between 12 and 20 wt%, which is in line with previous reports and what is typically observed for conventional activated carbons.[17,26–30] The yield is, however, higher than has been observed for carbonisation of other types of organic salts.[12] A better measure of the level of conversion of the C (51.3 wt%) component of PPI to the final carbonaceous matter is by considering the C yield, which also takes into account the C content of the PPI-derived carbons. As shown in Table 1, the C yield varies between 21 and 29 wt%. Although the C yield generally decreases at higher carbonisation temperature, the decrease is less than that observed for conventional activated carbons.[11,22–24,26–30]

The XRD patterns of the carbons (ESI, Fig. S1†) show broad and low-intensity peaks at $2\theta = 22°$ and $44°$, which is typical for such porous carbons. The peaks are indexed as (002), which is the diffraction plane of graphitic carbon for the interlayer spacing between adjacent graphite layers, and (100) that arises from in-plane ordering of graphite.[31] The broadness of the peaks and the low intensity of the (002) diffraction suggest that the carbons are essentially amorphous with a high level of irregularity. In this regard, the PPI-derived carbons are similar to those prepared from KHP and to activated carbons.[11,22–24,26–30]

To further probe the nature and elemental composition of the carbons, we performed X-ray photoelectron spectroscopy (XPS). The wide scan XPS spectra are shown in Fig. 1. The spectra show the presence of C, N and O in relative amounts consistent with the data in Table 1; the relative intensities of the peaks are in line with the elemental composition. In particular it is noted that while the C content increases with carbonisation temperature (Fig. 1 and ESI Fig. S2†), the N and O content decrease. Furthermore, the XPS spectra (Fig. 1 and ESI Fig. S2†) do not show the presence of K; the K 2p peak would be expected at *ca.* 293 eV. The absence of a K peak in the XPS spectra agrees with the XRD patterns (ESI Fig. S1†), which do not show any sharp peaks. Any residual K would exist in the form of crystalline K salts (*e.g.* K_2O and/or K_2CO_3) and which would give rise to sharp peaks in the XRD patterns. The absence of sharp peaks in the XRD patterns and non-appearance of the K peak in the XPS spectra confirm that the PPI-derived carbons do not have any residual K. High resolution N 1s XPS spectra (ESI Fig. S3†) show that the N environment in the carbons may be assigned to N-5 (pyrrolic/pyridonic) at 400.1 eV as the main component along with lower quantities of N-6 (pyridinic) at 398.6 eV, which is consistent with previous results on PPI-derived carbons.[17]

6954 | *J. Mater. Chem. A*, 2023, **11**, 6952–6965

This journal is © The Royal Society of Chemistry 2023

Table 1 Carbonisation yield and elemental composition of PPI-derived carbons

Sample	Yield [wt%]	Carbon yield (%)	C [wt%]	H [wt%]	N [wt%]	O [wt%]	O/C[a]
PPI[b]			51.3	2.1	7.4		0.26
PPI-600-2	20	29	73.2	1.0	5.3	20.5	0.21
PPI-700-2	17	25	76.3	0.8	2.6	20.3	0.20
PPI-800-2	16	27	87.6	0.2	1.8	10.4	0.09
PPI-900-2	13	23	90.5	0.1	1.3	8.1	0.07
PPI-1000-2	12	21	93.0	0.1	0.8	6.1	0.05

[a] Atomic ratio. [b] PPI also contains K (21.1 wt%) with the remainder being O (18.1 wt%).
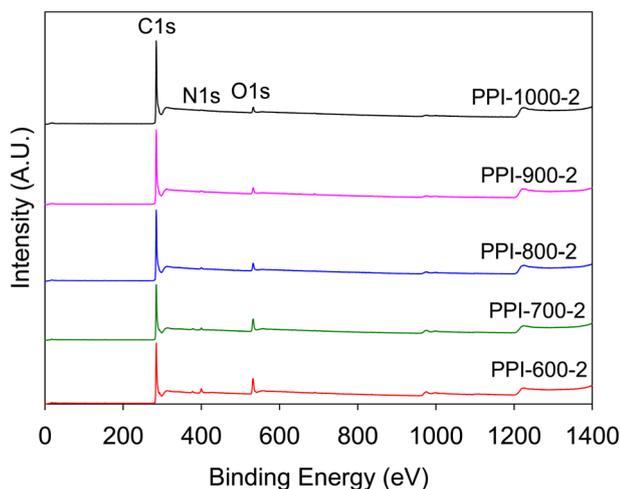

Fig. 1 X-ray photoelectron spectroscopy (XPS) wide scan spectra of PPI-derived carbons prepared *via* carbonisation for 2 h at 600 to 1000 °C.
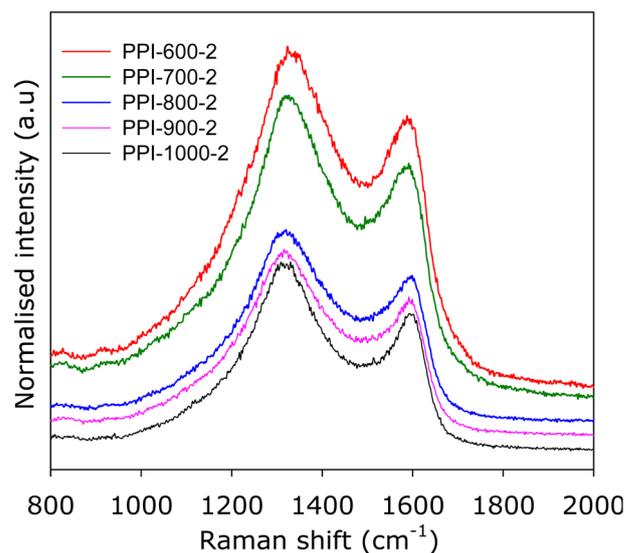

Fig. 2 Raman spectra of PPI-derived carbons prepared *via* carbonisation for 2 h at 600 to 1000 °C.

Further probing of the nature of the present carbons was obtained from Raman analysis. The Raman spectra are shown in Fig. 2, and exhibit bands centred at *ca.* 1330 cm^{-1} and 1590 cm^{-1} that are attributed, respectively, to the D-peak (disordered carbon) and the G-peak (graphitic domains).[32,33] The spectra, and in particular the ratio of peak intensity of the D-peak to G-peak (I_D/I_G), are comparable to those typically observed for activated carbons.[32,33] However, there appears to be a relatively weak correlation between the I_D/I_G ratio and carbonisation temperature, which implies that disorder increases as the severity of thermal treatment rises. Overall, however, the Raman spectra is consistent with the XRD patterns (ESI Fig. S1†) and mainly points to an amorphous nature for the PPI-derived carbons.

SEM analysis was used to probe the morphology of the PPI-derived carbons. The SEM images (ESI Fig. S4†) show platy particles with irregular shapes and sizes with holes randomly distributed across the surface. The presence of holes suggests that the porosity of the present carbons may in part be generated by gasification processes. Overall, it is interesting to note that the morphology is comparable to that typically observed for most activated carbons, while the platy nature of some particles has previously been reported for organic salt-derived carbons.[13–15] Graphene-like layers were not observed, indicating the amorphous nature of the carbon, in agreement with the XRD patterns (ESI Fig. S1†).

3.2 Porosity and textural properties

3.2.1 Effect of carbonisation temperature. The nitrogen sorption isotherms and pore size distribution (PSD) curves of the PPI-*T*-*y* carbons are shown in Fig. 3, and the corresponding textural properties are summarised in Table 2. All the isotherms are type I, indicating a microporous nature, which is desirable for small gas (CO_2 and CH_4) storage applications. All the isotherms have high nitrogen adsorption at $P/P_o < 0.1$, which points to high levels of microporosity. As the carbonisation temperature rises, the slope of the adsorption knee region (relative pressure range (P/P_o) of 0.01–0.3) increases slightly indicating that larger micropores are generated.[15] However, the isotherms remain comparable and representative of high microporosity even at the highest carbonisation temperature of 1000 °C. This means that whilst carbonisation temperature increases the overall porosity, this does not downgrade the level of microporosity. This contrasts with a previous report,[17] where higher carbonisation temperature generated carbons with lower

This journal is © The Royal Society of Chemistry 2023

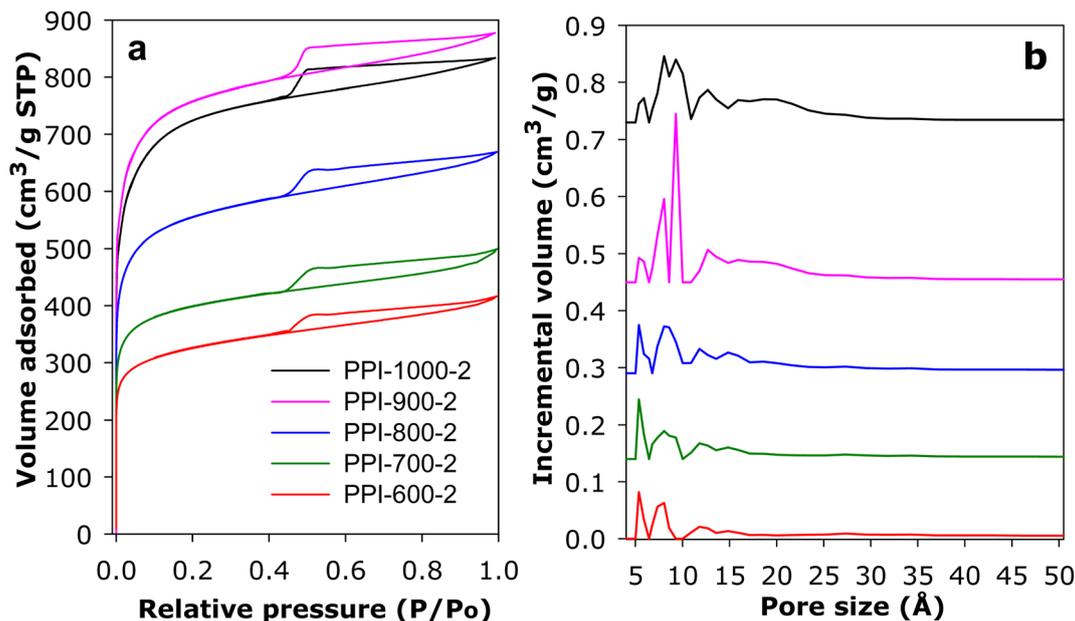*J. Mater. Chem. A*, 2023, **11**, 6952–6965 | **6955**

Fig. 3 (a) Nitrogen sorption isotherms and (b) pore size distribution (PSD) curves of PPI-derived carbons prepared *via* carbonisation for 2 h at 600 to 1000 °C.

levels of microporosity. We attribute this difference to washing the carbonised product with water, rather than acid as previously reported.[17] Washing with water is milder and allows for better retention of microporosity, which should also contribute to higher surface area for the final water washed carbons. The similarity in the shape of the isotherms also suggests that despite the wide range in the carbonisation temperature, the carbons all have a similar pore structure. This is a departure from what is observed for most activated carbons where, in general, higher activation temperatures lead to greater mesoporosity at the expense of microporosity.[22–24,26–30] In this regard, the PPI-derived carbons bear some similarity to KHP-derived carbons with respect to the limited effect of increasing the carbonisation temperature on the development of extensive mesoporosity.[11] The isotherms of all the samples exhibit a type H4 hysteresis loop that is consistent with the presence of both micropores and mesopores with the former being dominant.

As shown in Table 2, the surface area and pore volume increase with carbonisation temperature to a maximum at 900 °C; PPI-900-2 has high surface area and pore volume of 2889 m^2 g^{-1} and 1.36 cm^3 g^{-1}, respectively. The rise in porosity with increasing carbonisation temperature may be ascribed to higher levels of self-activation and pore development during thermal treatment of PPI. However, sample PPI-1000-2 exhibits a slightly lower surface area and pore volume compared to PPI-900-2, which may be ascribed to collapse of the structure due to possible overactivation involved the collapse of micropores into larger pores. Nevertheless, despite the wide range in overall porosity, all the carbons show a high level of microporosity with the proportion of micropore surface area and micropore volume at 81–89% and 66–77%, respectively. It is interesting to note that, instead of reducing, the proportion of micropore surface area and pore volume increase as the carbonisation temperature rises up to 900 °C. The present PPI-derived carbons achieve

Table 2 Textural properties of PPI-derived carbons prepared *via* carbonisation for 2 h at 600 to 1000 °C

Sample	Surface area (m^2 g^{-1})	Micropore surface area^a (m^2 g^{-1})	Pore volume (cm^3 g^{-1})	Micropore volume^b (cm^3 g^{-1})	Surf. area density^c (m^2 cm^{-3})	Packing density^d (g cm^{-3})	Vol. surface area^e (m^2 cm^{-3})
PPI-600-2	1227	1000 (82)	0.64	0.42 (66)	1917	1.10	1350
PPI-700-2	1517	1295 (85)	0.77	0.53 (69)	1970	1.04	1578
PPI-800-2	2106	1803 (86)	1.04	0.74 (71)	2025	0.92	1938
PPI-900-2	2889	2576 (89)	1.36	1.05 (77)	2124	0.87	2513
PPI-1000-2	2744	2410 (88)	1.29	0.95 (74)	2127	0.83	2278

^{a} Values in parenthesis are % of surface area from micropores. ^{b} Values in parenthesis are % of pore volume from micropores. ^{c} Surface area density is ratio of total surface area to total pore volume. ^{d} The experimentally determined packing density following compaction at 370 MPa. ^{e} Volumetric surface area determined as surface area × packing density.

6956 | *J. Mater. Chem. A*, 2023, **11**, 6952–6965

This journal is © The Royal Society of Chemistry 2023

much higher surface area and pore volume compared to that reported by Shi et al.[17] In particular, the surface area and pore volume of sample PPI-900-2, at close to 2900 $m^2 g^{-1}$ and 1.4 $cm^3 g^{-1}$, respectively, are higher by 40% (surface area) and 20% (pore volume). Furthermore, the level of microporosity is high regardless of carbonisation temperature, and greater than that reported by Shi et al.[17] The proportion of micropore surface area for the present PPI-derived carbons (81–89%) is higher than that (35–72%) reported by Shi et al.[17] There is a particularly large difference at 700, 800 and 900 °C, where the present PPI-derived carbons have, respectively, 85, 86 and 89% of surface area arising from micropores, compared to 62, 47 and 35%, respectively, as reported by Shi et al.[17] A similar picture is observed for the proportion of pore volume arising from micropores; 69, 71 and 77% for the present samples carbonised at 700, 800 and 900 °C, respectively, compared to 53, 39 and 28%, respectively, as reported by Shi et al.[17] We attribute the greater overall porosity and higher levels of microporosity to the use of water, rather than acid,[17] to wash the PPI-derived carbons after carbonisation. The use of water is not only simpler, cheaper and milder, but appears to be advantageous in achieving higher porosity along with greater levels of microporosity.

The pore size distribution (PSD) curves of PPI-T-2 samples (Fig. 3b and ESI Fig. S5†) confirm the relative similarity in their pore structure. At lower carbonisation temperature, the porosity of PPI-600-2, PPI-700-2 and PPI-800-2 is dominated by pores of size 5–8 Å. A slightly broader micropore size distribution is observed after carbonisation at 900 and 1000 °C (samples PPI-900-2 and PPI-1000-2) where it is likely that increasing gasification at the higher temperatures leads to larger micropores. We have previously shown that surface area density (SAD) of porous carbons, i.e., the ratio of total surface area to total pore volume, is related to the ratio of microporosity to mesoporosity, and that it may be used to predict the packing density of

a porous carbon.[9,24,26] As shown in Table 2, the SAD of the PPI-T-2 carbons is in the narrow range of 1917–2127 $m^2 cm^{-3}$, and which is generally higher than for most activated carbons.[27–30,33] Given the relatively high SAD, the expectation is that the PPI-derived carbons would have high packing density. We have previously shown that KHP-derived carbons can be readily compacted to a high packing density without any loss in textural properties.[11] The PPI-derived carbons were found to be similar as indicated by the packing density values of between 0.83–1.10 $g cm^{-3}$ (Table 2) following compacted at ambient temperature in a 1.3 cm (diameter) die for 10 min at 370 MPa. This indicates that the organic salt derived carbons are able to achieve comparatively high packing density relative to their overall porosity, which is beneficial in optimising volumetric surface area (Table 2) and more importantly volumetric gas uptake.[9,24,26] Interestingly, both surface area density and volumetric surface area increase with carbonisation temperature (and consequently overall porosity), which we ascribe to the fact that the extent of microporosity does not diminish as total porosity rises at higher carbonisation temperatures. This is the reverse of what is typically observed for conventional activated carbons and most other porous materials including MOFs.[27–30,33]

3.2.2 Effect of carbonisation time. Carbons were prepared at 700 and 800 °C for carbonisation durations of 1, 3 or 4 h to assess the effect of carbonisation time. The sorption isotherms of samples carbonised at 800 °C are shown in Fig. 4, and the corresponding textural properties are presented in Table 3. The isotherms are similar with respect to their shape, and are consistent with a high level of microporosity. As summarised in Table 3, the surface area and pore volume are only slightly affected by altering the carbonisation duration at 800 °C, but remain at 1928–2106 $m^2 g^{-1}$ and 0.86–1.04 $cm^3 g^{-1}$, respectively. Amongst PPI-800-y samples, PPI-800-2 has the highest
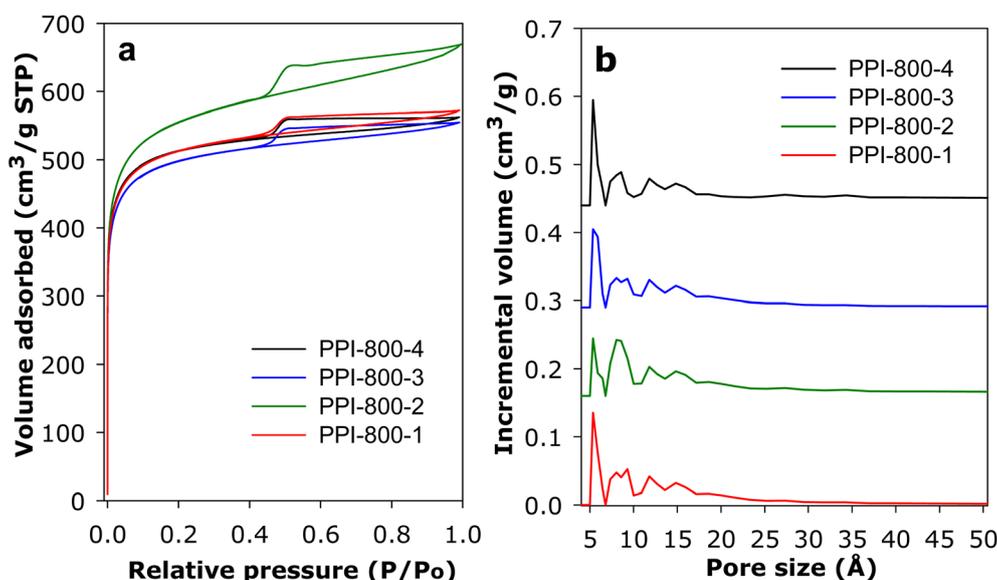

Fig. 4 (a) Nitrogen sorption isotherms and (b) pore size distribution (PSD) curves of PPI-derived carbons prepared via carbonisation at 800 °C for between 1 and 4 h.

This journal is © The Royal Society of Chemistry 2023

J. Mater. Chem. A, 2023, **11**, 6952–6965 | **6957**

Table 3 Textural properties of PPI-derived carbons carbonised at 800 °C and various periods of time

Sample	Surface area[a] ($m^2 g^{-1}$)	Pore volume[b] ($cm^3 g^{-1}$)	Pore size[c] (Å)
PPI-800-1	1976 (1804)	0.87 (0.73)	5, 8, 12, 15
PPI-800-2	2106 (1803)	1.04 (0.74)	5, 8, 12, 15
PPI-800-3	1928 (1768)	0.86 (0.71)	5, 8, 12, 15
PPI-800-4	1981 (1844)	0.87 (0.74)	5, 8, 12, 15

[a] The values in the parenthesis refer to micropore surface area. [b] The values in the parenthesis refer to micropore volume. [c] Main pore size maxima from PSD curves.

surface area and pore volume of 2106 $m^2 g^{-1}$ and 1.04 $cm^3 g^{-1}$, respectively. All PPI-800-y samples have a high proportion of micropore surface area (93%), while the proportion of micropore pore volume is in the range of 71–85%.

The pore size distribution curves in Fig. 4b show that the pore size is hardly affected by altering the carbonisation time at 800 °C; the maxima of pore size summarised in Table 3 are similar. Generally, carbonisation time 800 °C appears to have a negligible effect on the textural properties of the carbons. Hence, to generate porous carbons with attractive porosity and reduce the energy consumed, it is possible to carbonise PPI for 1 h without compromising the textural properties.

PPI-derived carbons were also prepared at 700 °C for 1, 3 or 4 h to clarify the role played by carbonisation temperature in determining the effects of carbonisation time. The nitrogen sorption isotherms and pore size distribution curves of PPI-700-y samples are shown in Fig. 5, and the corresponding textural properties are summarised in Table 4. The isotherms of PPI-700-y samples are similar and consistent with a high level of

microporosity. Compared to PPI-800-y samples, the PPI-700-y carbons exhibit a narrower pore size distribution. This confirms that a lower carbonisation temperature generates carbons with a narrower micropore size distribution but at lower surface area, ranging from 1502 to 1922 $m^2 g^{-1}$, whereas the pore volume varied between 0.67 and 0.85 $cm^3 g^{-1}$. PPI-700-y carbons show a high level of microporosity with 92% of surface area and 84% of pore volume arising from micropores regardless of the carbonisation duration.

3.3 Gas uptake measurements

3.3.1 CO$_2$ uptake. The CO_2 uptake isotherms of PPI-T-2 samples are shown in Fig. 6, and the uptake capacity at various pressures (0.15, 1 and 20 bar) is summarised in Table 5. The CO_2 uptake at 0.15 bar is a good indicator of performance for post-combustion CO_2 capture because flue gas streams from fossil fuel power stations contain *ca.* 15% CO_2, along with N_2 (70–75%), and water (5–7%). At 0.15 bar, PPI-600-2 and PPI-700-2 have high uptake of 1.6 and 1.5 mmol g^{-1}, respectively, due to the abundance of micropores of size *ca.* 8 Å (Fig. 3b). The other PPI-T-2 samples that have higher surface area but slightly broader pore size exhibit lower CO_2 uptake at 0.15 bar, which emphasises the importance of small micropores (6–8 Å) in the uptake of CO_2 at low pressure. It is, however, noteworthy that the CO_2 uptake of the present PPI-derived carbons at 0.15 bar (1.2–1.6 mmol g^{-1}) is higher than that previously reported (0.1–1.1 mmol g^{-1}) by Shi *et al.*[17] We attribute the higher uptake of the present carbons to greater levels of microporosity arising from a gentler and milder preparation route as discussed above.

The CO_2 uptake of PPI-T-2 carbons at 1 bar (Fig. 6b) is between 4.0 and 4.7 mmol g^{-1}, with the highest adsorption capacity being for sample PPI-700-2. The CO_2 uptake at 1 bar does not follow the trend in surface area, which once again
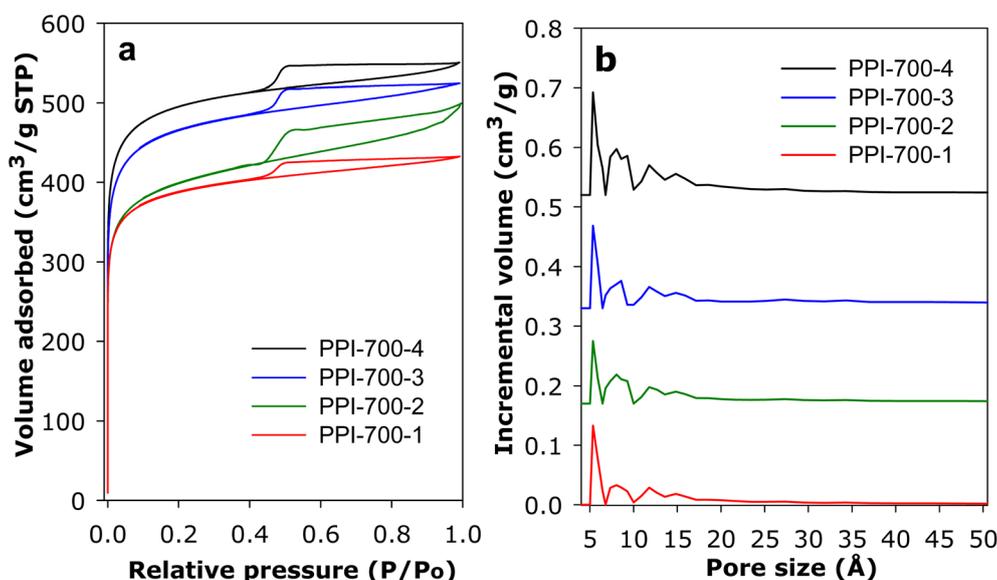

Fig. 5 (a) Nitrogen sorption isotherms and (b) pore size distribution (PSD) curves of PPI-derived carbons prepared *via* carbonisation at 700 °C for between 1 and 4 h.

6958 | *J. Mater. Chem. A*, 2023, **11**, 6952–6965

This journal is © The Royal Society of Chemistry 2023

Table 4 Textural properties of PPI-derived carbons carbonised at 700 °C and various periods of time

Sample	Surface area[a] ($m^2\ g^{-1}$)	Pore volume[b] ($cm^3\ g^{-1}$)	Pore size[c] (Å)
PPI-700-1	1502 (1367)	0.67 (0.55)	5, 8, 12
PPI-700-2	1517 (1295)	0.77 (0.53)	5, 8, 12
PPI-700-3	1790 (1612)	0.81 (0.65)	5, 8, 12
PPI-700-4	1922 (1773)	0.85 (0.71)	5, 8, 12

[a] The values in the parenthesis refer to micropore surface area. [b] The values in the parenthesis refer to micropore volume. [c] Main pore size maxima from PSD curves.
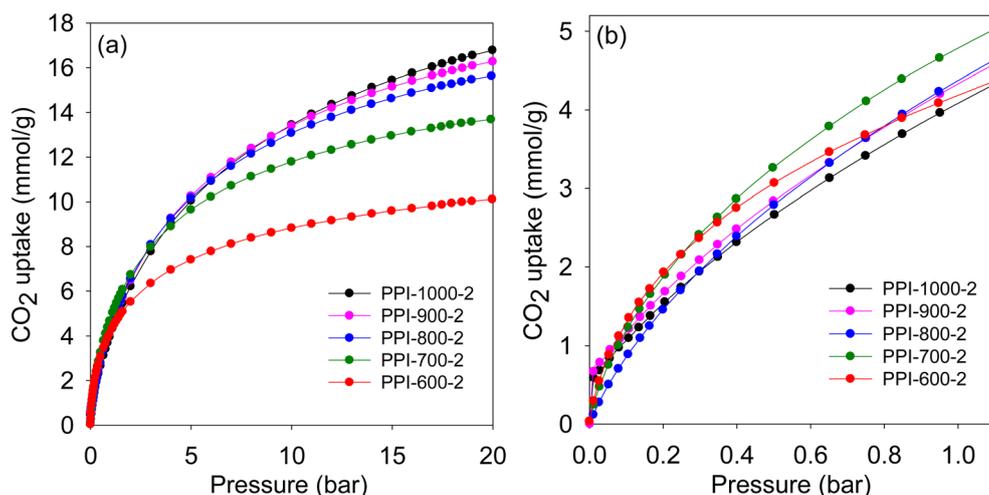

Fig. 6 CO_2 uptake isotherms at 25 °C and pressure of up to (a) 20 bar or (b) 1 bar for PPI-derived carbons carbonised at various temperatures for 2 h.

indicates that carbons must have optimised pores rather than just a high surface area to possess high CO_2 uptake at low pressure.[33–46] The CO_2 uptake of 4.7 mmol g^{-1} at 1 bar and 25 °C is comparable to the best activated carbons, but the current PPI-derived carbons have the advantage of being easy and simple to synthesise, as they only require the carbonisation process and no other chemical compounds than the precursor (PPI). This simpler preparation process yields carbons with better CO_2 uptake at 1 bar (4.1 mmol g^{-1} to 4.7 mmol g^{-1}) compared to that (3.1 mmol g^{-1} to 3.4 mmol g^{-1}) of equivalent PPI-derived carbons wherein acid was used during the washing step post carbonisation.[17] Although the CO_2 uptake at 1 bar for sample PPI-700-2 (4.7 mmol g^{-1}) is considerably higher than that of PPI-1000-2 (4.0 mmol g^{-1}), the trend is reversed at 20 bar, where

the former captures 16.8 mmol g^{-1} compared to 13.7 mmol g^{-1} for PPI-700-2. This shows that the CO_2 uptake at 20 bar relies more on the total surface area than the pore size. Notably, the CO_2 uptake isotherms of PPI-600-2 and PPI-700-2 appear to approach saturation at 20 bar whilst samples with a slightly wider pore size (PPI-800-2, PPI-900-2 and PPI-1000-2) are far from saturation, suggesting that more CO_2 can be stored at higher pressures.

While there is a clear trend between the pore size and CO_2 uptake at low pressure, we did not observe any clear positive effect of the N content. This is consistent with previous reports that the CO_2 uptake of carbons at low pressure is mainly dependent on porosity, and in particular pore size, rather than N content.[37] However, this does not rule out the possibility that the presence of N may affect the isosteric heat of CO_2 adsorption. Given the highly microporous nature of the present carbons and the fact that they possess significant amounts of N, it was interesting to determine the isosteric heat of CO_2 adsorption (Q_{st}). Pores of size < 10 Å and the presence of N in carbon frameworks are considered to be contributors to enhanced CO_2 adsorption in porous carbons. The carbons have Q_{st} in the range of 36–20 kJ mol^{-1} (ESI Fig. S6†), which is higher than previously reported to acid-washed PPI-derived carbons.[17] This is not unexpected given that the present water-washed carbons have much higher levels of microporosity.

Table 5 CO_2 uptake at 25 °C of PPI-derived carbons carbonised at various temperatures for 2 h

Sample	CO_2 uptake (mmol g^{-1})		
	0.15 bar	1 bar	20 bar
PPI-600-2	1.6	4.1	10.1
PPI-700-2	1.5	4.7	13.7
PPI-800-2	1.2	4.2	15.7
PPI-900-2	1.4	4.2	16.3
PPI-1000-2	1.2	4.0	16.8

This journal is © The Royal Society of Chemistry 2023

J. Mater. Chem. A, 2023, **11**, 6952–6965 | **6959**

As discussed above, the textural properties of PPI-derived carbons are not significantly affected by changing the carbonisation duration (in the range 1 to 4 h) at 800 °C. As presented in Fig. 7a, b and Table 6, the comparable CO_2 uptake at various pressures for PPI-800-y samples is consistent with their relatively similar textural properties. In contrast, the PPI-700-y samples (Fig. 7c, d and Table 6) show similar CO_2 uptake at 0.15 bar and 1 bar (1.5–1.7 mmol g^{-1}) and (4.7–5.2 mmol g^{-1}), respectively, but show a broader variation at 20 bar (12.9–15.7 mmol g^{-1}). The uptake of 1.7 mmol g^{-1} at 0.15 bar and 5.2 mmol g^{-1} at 1 bar are amongst the highest ever reported for porous carbon material.[33–41] The greater spread of uptake at 20 bar is in line with the trend in total surface area. The CO_2 uptake data shows that there are opportunities to optimise performance by varying the carbonisation duration and consequently the porosity. However, overall, the changes in CO_2 uptake are limited and therefore carbonisation duration of 1 h can be considered as being sufficient.

Post-combustion CO_2 capture involves flue gas streams whose other main constituent is N_2. This means that the extent to which any adsorbents are selective towards adsorbing CO_2 over N_2 is an important consideration. We therefore determined the selectivity of two of the high performing carbons (PPI-700-2 and PPI-700-3) by comparing their uptake for CO_2 and N_2 at 25 °C and 1 bar. The comparison (ESI Fig. S7†) shows that the uptake at 1 bar is as follows; 0.19 mmol per g N_2 and 4.7 mmol per g CO_2 for PPI-700-2, and 0.21 mmol per g N_2 and 5.2 mmol per g CO_2 for PPI-700-3. This gives a high equilibrium CO_2/N_2 adsorption ratio of 25 for both PPI-700-2 and PPI-700-3, compared to values typically less than 15 for most activated carbons.[34] The selectivity for CO_2 may also be estimated from a simulated post-combustion flue gas stream containing 15% CO_2 and 85% N_2 by comparing the relative uptake of the gases at 0.15 bar for CO_2 and 0.85 bar for N_2. In this case, the determination of selectivity is according to the ideal adsorbed solution theory (IAST), which is useful for estimating the selectivity by any adsorbent for any two given gases in a binary gas mixture
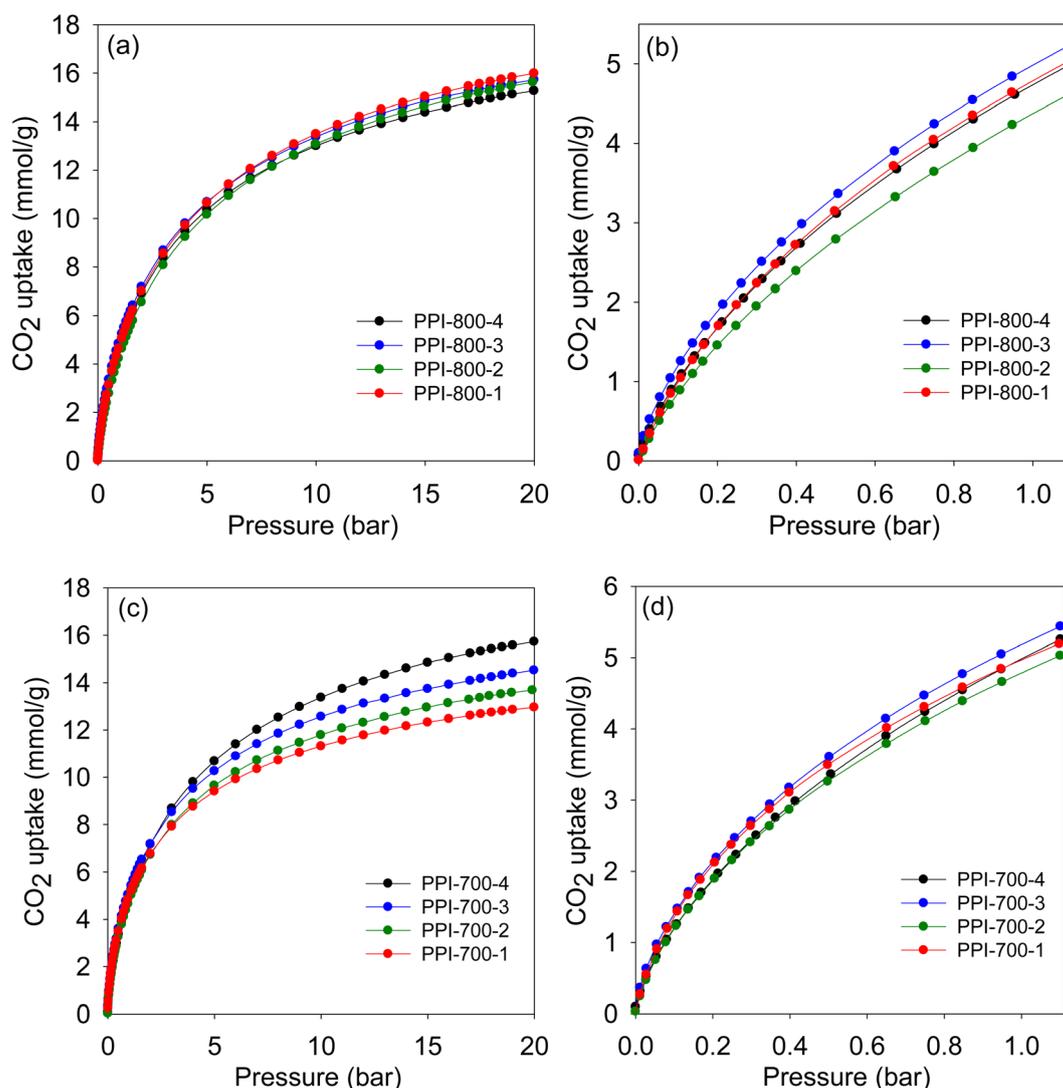

Fig. 7 CO_2 uptake isotherms of PPI-derived carbons carbonised at 800 °C (a and b) or 700 °C (c and d) for various periods of time.

6960 | J. Mater. Chem. A, 2023, **11**, 6952–6965

This journal is © The Royal Society of Chemistry 2023

Table 6 CO_2 uptake of PPI-derived carbons carbonised at 800 °C or 700 °C for various periods of time

Sample	CO_2 uptake (mmol g^{-1})		
	0.15 bar	1 bar	20 bar
PPI-800-1	1.3	4.6	16.0
PPI-800-2	1.2	4.2	15.7
PPI-800-3	1.5	4.8	15.7
PPI-800-4	1.3	4.6	15.3
PPI-700-1	1.7	4.8	12.9
PPI-700-2	1.5	4.7	13.7
PPI-700-3	1.7	5.2	14.5
PPI-700-4	1.5	4.8	15.7

according to the equation; $S = n(CO_2)\,p(N_2)/n(N_2)\,p(CO_2)$, where $n(CO_2)$ is CO_2 uptake at 0.15 bar, $n(N_2)$ is N_2 uptake at 0.85 bar, $p(N_2)$ is 0.85 and $p(CO_2)$ is 0.15. For PPI-700-2 and PPI-700-3 (ESI Fig. S7†), this determination yields very high selectivity of 52 and 50 for PPI-700-2 and PPI-700-3, respectively.

The high microporosity of the present carbons means that they are best suited for post-combustion CO_2 uptake where they perform better that most previously reported porous carbons (ESI Table S1†). To get a fuller picture of the performance of the carbons, and given their relatively high packing density, we determined their volumetric CO_2 uptake at pressure of up to 9 bar (ESI Table S2†). Volumetric uptake is dependent on the gravimetric storage capacity and the packing density. The volumetric uptake of the PPI-derived carbons (ESI Table S2†) is very attractive and compares favourably with or outperforms that previously reported for benchmark materials – carbons[33–46] or MOFs.[47–49] The best all round performance is for sample PPI-700-2, which achieves CO_2 uptake of 62 g l^{-1} (35 cm³ cm⁻³) at 0.15 bar, 196 g l^{-1} (110 cm³ cm⁻³) at 1 bar, 401 g l^{-1} (225 cm³ cm⁻³) at 5 bar, and 477 g l^{-1} (267 cm³ cm⁻³) at 9 bar.

Given that post-combustion CO_2 capture would proceed *via* adsorption and regeneration cycles, we determined the amount that would be sequestered (*i.e.*, working capacity) for pressure swing operations in either a pressure swing adsorption (PSA) process or a vacuum swing adsorption (VSA) process.[50] To mimic likely real use conditions we considered the following scenarios; adsorption at 6 bar and desorption at 1 bar for PSA, and adsorption at 1.5 bar and desorption at 0.05 bar for VSA.[50] Given that fossil fuel power station flue gas streams contain less than 20% CO_2, we also determined the working capacity from such a stream (*i.e.* 20% CO_2). The working capacity of the present carbons is given in Table 7, which also includes previously reported data for high performing carbons,[9,35] MOFs (Mg-MOF-74 and HKUST-1),[51] and zeolite NaX.[52] The PSA working capacity of the PPI-derived carbons is between 3.7 and 7.0 mmol g^{-1} for a pure CO_2 stream. This performance is comparable or better than that of the best carbons (3.4–8.1 mmol g^{-1}) or MOFs, namely, HKUST-1 (7.8 mmol g^{-1}) and Mg-MOF-74 (3.5 mmol g^{-1}), and is higher than for zeolite NaX (1.6 mmol g^{-1}). The PSA working capacity for flue gas conditions ranges between 2.6 and 3.4 mmol g^{-1}, which is comparable to that of current benchmark carbons (3.0–4.1 mmol g^{-1}) and HKUST-1

Table 7 Gravimetric working capacity for pressure swing adsorption (PSA) and vacuum swing adsorption (VSA) of CO_2 on PPI-derived carbons compared to benchmark porous materials at 25 °C for a pure CO_2 gas stream and a 20% partial CO_2 pressure flue gas stream

Sample	Pure CO_2 uptake[a] (mmol g^{-1})		Flue gas CO_2 uptake[b] (mmol g^{-1})		Reference
	PSA	VSA	PSA	VSA	
PPI-600-2	3.7	4.1	2.6	2.4	This work
PPI-700-2	5.5	5.1	3.3	2.4	This work
PPI-800-2	6.7	5.1	3.4	1.9	This work
PPI-900-2	6.9	4.6	3.1	2.1	This work
PPI-1000-2	7.0	4.4	3.0	1.9	This work
ACC2700	7.4	5.8	4.0	1.9	9
ACC2800	7.8	5.1	3.5	1.6	9
HCC2700	6.5	6.1	4.2	2.3	9
HCC2800	8.1	5.2	3.6	1.7	9
SD2600	3.7	4.6	3.0	2.1	35
SD2600P	3.4	6.0	4.1	2.9	35
SD2650	3.8	4.6	3.1	1.9	35
SD2650P	4.0	5.7	4.0	2.4	35
HKUST-1	7.8	6.4	4.5	1.6	51
Mg-MOF-74	3.5	3.9	2.1	4.1	51
NaX	1.6	2.8	1.8	2.5	52

[a] 1 bar to 6 bar for PSA; 0.05 bar to 1.5 bar for VSA. [b] 0.2 bar to 1.2 bar for PSA; 0.01 bar to 0.3 bar for VSA.

(4.5 mmol g^{-1}). The same trends and attractive performance are observed for VSA working capacity. Furthermore, the high packing density of the PPI-derived carbons means that they achieve excellent volumetric working capacity for PSA and VSA processes (ESI Table S3†), which is in some cases more than double that of the benchmark MOFs.

3.3.2 Methane storage. The microporosity of porous materials with a high surface area along with low mesoporosity are critical requirements for methane storage at moderate to high pressure (35–100 bar).[1–4,9,24,26,53] A high micropore volume is required to ensure strong adsorption of methane molecules, while some mesoporosity is necessary for effective sorption kinetics. Therefore, the mix of porosity of the PPI-derived carbons is attractive for attaining high methane storage at moderate pressures. Given the importance of overall surface area and pore volume in determining methane uptake,[1–5,9,24,26] we only explored the performance of PPI-derived carbons that have high surface area (*i.e.*, > 2000 m² g^{-1}), namely, PPI-800-2, PPI-900-2 and PPI-1000-2. Our methane uptake measurements directly determined the excess uptake from which the total storage capacity could be worked out by considering the methane density at any particular temperature and pressure, and the total pore volume of the adsorbing carbon using the equation; $\theta_T = \theta_{Exc} + d_{CH_4} \times V_T$, where θ_T is the total methane uptake, θ_{Exc} is the excess methane uptake, d_{CH_4} is the methane gas density (g cm⁻³), which is available from the National Institute of Standards and Technology website (https://www.nist.gov/), and V_T is total pore volume (cm³ g^{-1}) of the adsorbing carbon.

This journal is © The Royal Society of Chemistry 2023

J. Mater. Chem. A, 2023, **11**, 6952–6965 | **6961**

Fig. 8 shows the excess and total methane uptake isotherms, and Table 8 presents the respective storage capacity at 35, 65 and 100 bar. The excess methane isotherm of PPI-1000-2 does not appear to reach saturation at 100 bar while PPI-900-2 and PPI-800-2 reach maxima at 65 to 80 bar (Fig. 8). This behaviour is commonly observed during high pressure adsorption of supercritical fluids, and results from a scenario where the density of bulk or free methane is equal to the density of adsorbed methane.[54,55] The excess uptake remains unchanged at pressures above the maximum, which for PPI-800-2 and PPI-900-2 is 10.1 and 10.5 mmol g^{-1}, respectively. For sample PPI-1000-2, the excess uptake remains virtually constant (*ca.* 12.1 mmol g^{-1}) between 80 and 100 bar with a likely maxima at *ca.* 100 bar where it has been reported to occur for some shale samples.[54–56] The excess methane uptake is therefore in line with the porosity with samples having a high surface area and pore volume showing better uptake. Surprisingly, for organic-salt-derived carbons, the excess methane uptake of up to 10.3 mmol g^{-1} (0.165 g g^{-1}) at 35 bar and 25 °C is comparable to the best porous materials.[1–5,53,57,58] The excess uptake rises to up to 12 mmol g^{-1} at 100 bar. The total methane uptake at 35 bar ranges from 10.9 to 12.0 mmol g^{-1} (0.17–0.19 g g^{-1}), and increases to 13.5–15.5 mmol g^{-1} at 65 bar, and 15.0 to 18.2 mmol g^{-1} at 100 bar (Table 8). Fig. 9 shows the isosteric heat of methane adsorption (Q_{st}) for the carbons as a function of methane loading. The Q_{st} is between 21 and 15 kJ mol^{-1} for methane loading of up to 7 mmol g^{-1}. The observed Q_{st} is within the range typically observed for activated carbons, *i.e.*, 10–25 kJ mol^{-1} depending on methane loading.[59]

Volumetric uptake is the critical measure of a solid's performance in methane storage. According to the US Department of Energy (DOE), the volumetric methane storage target in porous materials is 263 cm^3 (STP) cm^{-3} at moderate pressure (35–100 bar) and room temperature (25 °C).[1–4] The high packing

Table 8 Excess and total gravimetric methane uptake at 25 °C for PPI-derived carbons

| | Gravimetric methane uptake (mmol g^{-1}) | | | | | |
| | Excess uptake | | | Total uptake | | |
Sample	35 bar	65 bar	100 bar	35 bar	65 bar	100 bar
PPI-800-2	9.4	10.1	10.1	10.9	13.1	15.0
PPI-900-2	9.9	10.5	10.5	11.8	14.5	17.0
PPI-1000-2	10.3	11.7	12.1	12.0	15.5	18.2

density of the PPI-derived carbons, along with their attractive gravimetric uptake, should translate to excellent volumetric uptake. A high packing density is critical in optimising volumetric uptake in the sense that having more (with respect to mass) of an adsorbent in any restricted volume will act to enhance gas uptake. The self-activating nature of the present PPI-derived carbons, and the fact that they are highly microporous means that their packing density (Table 2) is high with the consequence that they maintain high performance with respect to volumetric uptake of methane as shown in Fig. 10 and summarised in Table 9. The carbons have volumetric uptake of 224 to 230 cm^3 (STP) cm^{-3} at 35 bar and 25 °C, which is remarkable in the context of previous reports for carbons and other porous materials.[1–5,9,24,26,57–62] The performance of the PPI-derived carbons is comparable to that of the best-performing porous carbons to date, *i.e.*, activated carbons derived from date seeds (*Phoenix dactylifera*) or cloves, which store up to 222 or 235 cm^3 (STP) cm^{-3}, respectively, at 25 °C and 35 bar.[9,26] The performance of the PPI-derived carbons is comparable to the best MOF reported to date, *i.e.*, $_{mono}$HKUST-1, which can store 224 cm^3 (STP) cm^{-3} at 25 °C and 35 bar.[63] $_{mono}$HKUST-1, which exists in monolithic form, is reported to have packing density of 1.06 g cm^{-3} and is considered to be the benchmark material for
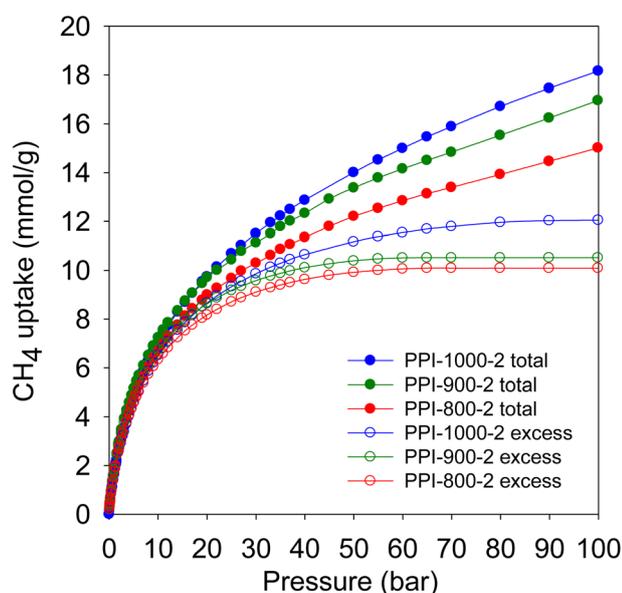

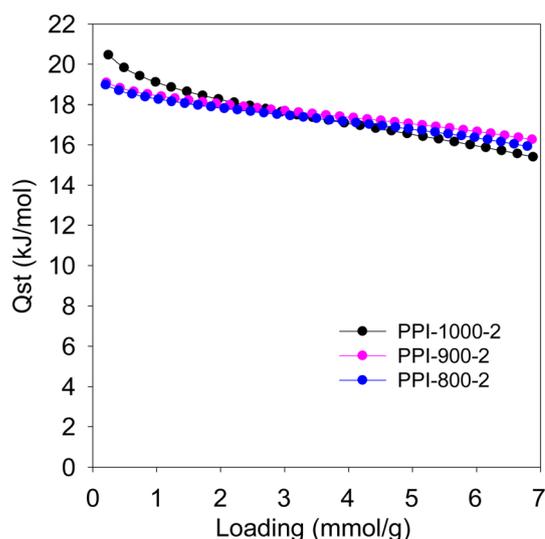**Fig. 8** Excess and total gravimetric methane uptake at 25 °C for PPI-derived carbons.

Fig. 9 Isosteric heat of adsorption (Q_{st}) of methane on PPI-derived carbons prepared *via* carbonisation for 2 h at 800 to 1000 °C.
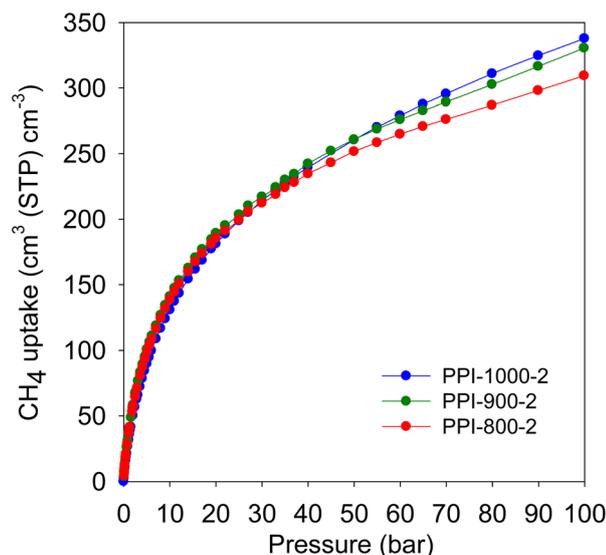
6962 | *J. Mater. Chem. A*, 2023, **11**, 6952–6965

This journal is © The Royal Society of Chemistry 2023

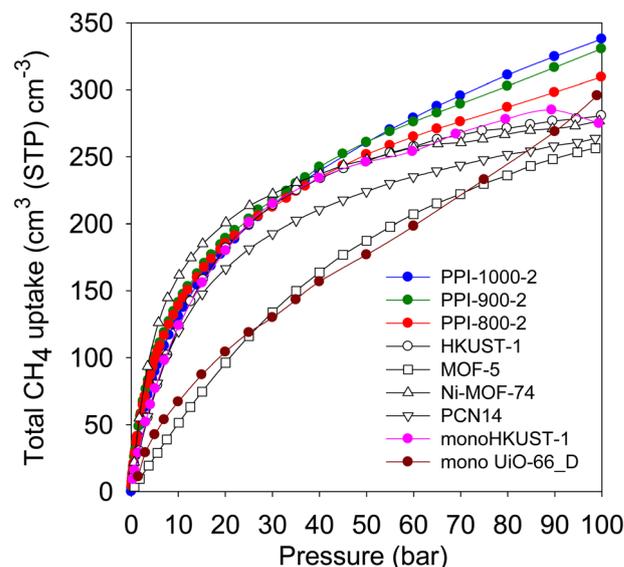Fig. 10 Total volumetric methane uptake of PPI-derived carbons at 25 °C.

Fig. 11 Total volumetric methane uptake of PPI-derived carbons at 25 °C compared to benchmark MOF materials. The uptake of powder MOFs was calculated using their crystal density.

volumetric methane storage in MOFs materials.[63] The total methane uptake increases to between 271 and 288 cm³ (STP) cm⁻³ at 65 bar, and is exceptionally high (309–338 cm³ (STP) cm⁻³) at 100 bar. The isotherms in Fig. 10 indicate that the volumetric uptake reaches or surpasses the DOE target (263 cm³ (STP) cm⁻³) at 60 bar for PPI-800-2 and 50 bar for PPI-900-2 and PPI-1000-2. This means that the uptake of the PPI carbons at 100 bar surpasses, by some margin, the DOE target.

Fig. 11 shows how the performance of the PPI-derived carbons compares with the best reported powder MOFs (HKUST-1, MOF-5, Ni-MOF-74 and PCN-14)[64,65] and monolithic MOFs (monoHKUST-1 and monoUiO-66_D).[63,66] It is important to note that the volumetric uptake of the powder MOFs is calculated using crystal density, which is known to overestimate the uptake capacity. Given that the actual packing density of powder MOFs is significantly lower than the crystal density, a more realistic comparison is to allow for at least a 25% reduction in the crystal density-based calculated uptake to take into account the expected loss in packing density (ESI Fig. S8†). The performance of the PPI-derived carbons is also benchmarked (ESI Table S4†) against other leading MOFs (including

Al-soc-MOF-1, MOF-210, NU-1500-Al, NU-1501-Fe and NU-1501-Al) and carbon materials.[1–5,9,24,26,48,67,68] The volumetric uptake of the present carbons surpasses that of all powder MOFs and is comparable to the best carbons (Fig. 11, ESI Fig. S8 and ESI Table S4†). Comparison with monoHKUST-1 and monoUiO-66_D, is more realistic as it excludes the uncertainty of the use of crystal density. The PPI-derived carbons outperform the monolithic MOFs at pressure above 40 bar, which are the most relevant for methane (or natural gas) storage for vehicular use.

Working capacity is a critical measure of the performance of a porous material in methane storage, and is defined as the difference in the uptake between the adsorption and desorption pressures. A desorption (or delivery) pressure of ca. 5 bar is recommended for methane storage, whereas an adsorption pressure of 35 bar or above has been used in this study. Table 9 shows the volumetric working capacity of the PPI-derived carbons. For a 35 to 5 bar pressure swing, the working capacity is in the range of 127 to 138 cm³ cm⁻³, which is comparable to the highest values previously reported for any porous materials.[9,24,26] The working capacity is even more impressive at uptake pressure of 65 bar and above as shown in Table 9, reaching 199 and 249 cm³ cm⁻³, respectively, for swings of 65 to 5 bar, and 100 to 5 bar. Such performance is superior to all previously reported MOFs and comparable to the best carbons (ESI Table S5†). Nevertheless, it should be noted that the values for powder MOFs (ESI Table S5†) are calculated using crystal density and thus likely to be overestimated. A more realistic comparison is with the monolithic MOFs, namely, monoHKUST-1 and monoUiO-66_D, to which the PPI-derived carbons are comparable. This means that the present carbons are very attractive given that the monolithic MOFs are claimed to be 50% better than any other MOF in terms of volumetric uptake.[63,66] A further consideration is the simplicity and cost of

Table 9 Total volumetric methane uptake and working capacity for PPI-derived carbons

Sample	Total volumetric uptake (cm³ (STP) cm⁻³)			Working capacity[a] (cm³ (STP) cm⁻³)		
	35 bar	65 bar	100 bar	35 bar	65 bar	100 bar
PPI-800-2	224	271	309	127	174	212
PPI-900-2	230	283	331	130	183	231
PPI-1000-2	227	288	338	138	199	249

[a] The volumetric working capacity is defined as the difference in uptake between the stated pressure (35, 65 or 100 bar) and 5 bar.

This journal is © The Royal Society of Chemistry 2023

J. Mater. Chem. A, 2023, **11**, 6952–6965 | **6963**

preparation of the PPI-derived carbons compared to MOFs (in powder or monolithic form), and porous carbons whether templated carbons[69,70] or conventional activated carbons.

4   Conclusion

Porous carbons were successfully prepared by heating a carbon-rich organic salt, namely, potassium phthalimide (PPI) at 600–1000 °C, followed by washing with deionised water. The PPI-derived carbons presented a high carbon content, which rises with carbonisation temperature from 73–93 wt%, compared to 51 wt% for PPI. As a consequence, the H, N and O content of the carbons decrease with the increase in the carbonisation temperature but all samples still retain some N (0.8–5.3 wt%). The carbons have high surface area and pore volume (up to 2889 m^2 g^{-1} and 1.36 cm^3 g^{-1}, respectively, for a sample carbonised at 900 °C for 2 h), and have high levels of microporosity (80–90% of surface area) regardless of the carbonisation temperature. The porosity is dominated by micropores (5–15 Å), which is advantageous for CO_2 and methane uptake. At 25 °C, the PPI-derived carbons capture up to 1.7 and 5.2 mmol g^{-1} of CO_2 at 0.15 and 1 bar, respectively, with excellent total volumetric uptake and impressive working capacity for pressure swing adsorption processes aligned to post-combustion CO_2 capture. The PPI-derived carbons have volumetric methane uptake of up to 338 cm^3 (STP) cm^{-3} at 100 bar and 25 °C, which surpasses the target set by the US DOE (263 cm^3 (STP) cm^{-3}). Crucially, the DOE target is surpassed at uptake pressures as low as 50 bar. The high uptake is accompanied by impressive working capacity that reaches 249 cm^3 (STP) cm^{-3} for the pressure swing of 100 bar (uptake pressure) to 5 bar (desorption or delivery pressure). According to the findings of this study, PPI is an attractive precursor for the simple synthesis of porous carbons with a mix of properties suited for enhanced CO_2 and methane storage applications.

Author contributions

Ibtisam Alali: methodology, formal analysis, Investigation, writing. Robert Mokaya: conceptualisation, writing – review & editing, supervision, funding acquisition, resources.

Conflicts of interest

There are no conflicts to declare.

Acknowledgements

References

1 Y. He, W. Zhou, G. Qian and B. Chen, *Chem. Soc. Rev.*, 2014, **43**, 5657–5678.

2 T. A. Makal, J. R. Li, W. Lu and H. C. Zhou, *Chem. Soc. Rev.*, 2012, **41**, 7761–7779.

3 J. A. Mason, M. Veenstra and J. R. Long, *Chem. Sci.*, 2014, **5**, 32–51.

4 B. Li, H. M. Wen, W. Zhou, J. Q. Xu and B. Chen, *Chem*, 2016, **1**, 557–580.

5 M. E. Casco, M. Martínez-Escandell, E. Gadea-Ramos, K. Kaneko, J. Silvestre-Albero and F. Rodríguez-Reinoso, *Chem. Mater.*, 2015, **27**, 959–964.

6 M. K. Antoniou, E. K. Diamanti, A. Enotiadis, A. Policicchio, K. Dimos, F. Ciuchi, E. Maccallini, D. Gournis and R. G. Agostino, *Microporous Mesoporous Mater.*, 2014, **188**, 16–22.

7 S. Ma and H. C. Zhou, *Chem. Commun.*, 2010, **46**, 44–53.

8 L. S. Blankenship and R. Mokaya, *Mater. Adv.*, 2022, **3**, 1905–1930.

9 I. Alali and R. Mokaya, *Energy Environ. Sci.*, 2022, **15**, 4710–4724.

10 M. Sevilla and R. Mokaya, *Energy Environ. Sci.*, 2014, 7, 1250–1280.

11 B. Adeniran, E. Masika and R. Mokaya, *J. Mater. Chem. A*, 2014, **2**, 14696–14710.

12 J. D. Atkinson and M. J. Rood, *Microporous Mesoporous Mater.*, 2012, **160**, 174–181.

13 M. Sevilla and A. B. Fuertes, *J. Mater. Chem. A*, 2013, **1**, 13738–13741.

14 M. Sevilla and A. B. Fuertes, *ACS Nano*, 2014, **8**, 5069–5078.

15 E. Masika and R. Mokaya, *RSC Adv.*, 2013, **3**, 17677–17681.

16 Q. Zhang, B. Yan, L. Feng, J. Zheng, B. You, J. Chen, X. Zhao, C. Zhang, S. Jiang and S. He, *Nanoscale*, 2022, **14**, 8216–8244.

17 J. Shi, H. Cui, J. Xu, N. Yan, Y. Liu and S. Zhang, *J. CO2 Util.*, 2020, **39**, 101164.

18 L. Wei, M. Sevilla, A. B. Fuertes, R. Mokaya and G. Yushin, *Adv. Funct. Mater.*, 2012, **22**, 827–834.

19 M. Sevilla, R. Mokaya and A. B. Fuertes, *Energy Environ. Sci.*, 2011, **4**, 2930–2936.

20 M. Cox and R. Mokaya, *Sustainable Energy Fuels*, 2017, **1**, 1414–1424.

21 J. S. M. Lee, M. E. Briggs, T. Hasell and A. I. Cooper, *Adv. Mater.*, 2016, **28**, 9804–9810.

22 B. Adeniran and R. Mokaya, *Nano Energy*, 2015, **16**, 173–185.

23 N. Balahmar and R. Mokaya, *J. Mater. Chem. A*, 2019, **7**, 17466–17479.

24 A. Altwala and R. Mokaya, *J. Mater. Chem. A*, 2022, **10**, 13744–13757.

25 F. Rouquerol, J. Rouquerol and K. Sing, *Adsorption by Powders and Porous Solids: Principles, Methodology and Applications*, Academic Press, San Diego, 1999.

26 A. Altwala and R. Mokaya, *Energy Environ. Sci.*, 2020, **13**, 2967–2978.

27 A. M. Aljumialy and R. Mokaya, *Mater. Adv.*, 2020, **1**, 3267–3280.

6964 | *J. Mater. Chem. A*, 2023, **11**, 6952–6965

This journal is © The Royal Society of Chemistry 2023

28 M. Sevilla, A. B. Fuertes and R. Mokaya, *Energy Environ. Sci.*, 2011, **4**, 1400–1410.

29 N. Balahmar, A. S. Al-Jumialy and R. Mokaya, *J. Mater. Chem. A*, 2017, **5**, 12330–12339.

30 H. M. Coromina, D. A. Walsh and R. Mokaya, *J. Mater. Chem. A*, 2015, **4**, 280–289.

31 C. Yuan, X. Liu, M. Jia, Z. Luo and J. Yao, *J. Mater. Chem. A*, 2015, **3**, 3409–3415.

32 E. A. Hirst, A. Taylor and R. Mokaya, *J. Mater. Chem. A*, 2018, **6**, 12393–12403.

33 W. Sangchoom and R. Mokaya, *ACS Sustainable Chem. Eng.*, 2015, **3**, 1658–1667.

34 M. Sevilla and A. B. Fuertes, *Energy Environ. Sci.*, 2011, **4**, 1765–1771.

35 N. Balahmar, A. C. Mitchell and R. Mokaya, *Adv. Energy Mater.*, 2015, **5**, 1500867.

36 J. P. Marco-Lozar, M. Kunowsky, F. Suárez-García, J. D. Carruthers and A. Linares-Solano, *Energy Environ. Sci.*, 2012, **5**, 9833–9842.

37 B. Adeniran and R. Mokaya, *Chem. Mater.*, 2016, **28**, 994–1001.

38 Z. Zhang, J. Zhou, W. Xing, Q. Xue, Z. Yan, S. Zhuo and S. Z. Qiao, *Phys. Chem. Chem. Phys.*, 2013, **15**, 2523–2529.

39 E. Haffner-Staton, N. Balahmar and R. Mokaya, *J. Mater. Chem. A*, 2016, **4**, 13324–13335.

40 N. P. Wickramaratne and M. Jaroniec, *J. Mater. Chem. A*, 2013, **1**, 112–116.

41 A. Altwala and R. Mokaya, *Energy Advances*, 2022, **1**, 216–224.

42 N. P. Wickramaratne and M. Jaroniec, *ACS Appl. Mater. Interfaces*, 2013, **5**, 1849–1855.

43 J. Silvestre-Albero, A. Wahby, A. Sepúlveda-Escribano, M. Martínez-Escandell, K. Kaneko and F. Rodríguez-Reinoso, *Chem. Commun.*, 2011, **47**, 6840–6842.

44 A. Altwala and R. Mokaya, *RSC Adv.*, 2022, **12**, 20080–20087.

45 A. Wahby, J. M. Ramos-Fernández, M. Martínez-Escandell, A. Sepúveda-Escribano, J. Silvestre-Albero and F. Rodríguez-Reinoso, *ChemSusChem*, 2010, **3**, 974–981.

46 L. S. Blankenship, N. Albeladi, T. Alkhaldi, A. Madkhali and R. Mokaya, *Energy Advances*, 2022, **1**, 1009–1020.

47 S. R. Caskey, A. G. Wong-Foy and A. J. Matzger, *J. Am. Chem. Soc.*, 2008, **130**, 10870–10871.

48 H. Furukawa, N. Ko, Y. B. Go, N. Aratani, S. B. Choi, E. Choi, A. O. Yazaydin, R. Q. Snurr, M. O'Keeffe, J. Kim and O. M. Yaghi, *Science*, 2010, **329**, 424–428.

49 Y. Peng, V. Krungleviciute, I. Eryazici, J. T. Hupp, O. K. Farha and T. Yildirim, *J. Am. Chem. Soc.*, 2013, **135**, 11887–11894.

50 L. Wang, Y. Yang, W. Shen, X. Kong, P. Li, J. Yu and A. E. Rodrigues, *Ind. Eng. Chem. Res.*, 2013, **52**, 7947–7955.

51 J. M. Simmons, H. Wu, W. Zhou and T. Yildirim, *Energy Environ. Sci.*, 2011, **4**, 2177–2185.

52 Y. Belmabkhout, G. Pirngruber, E. Jolimaitre and A. Methivier, *Adsorption*, 2007, **13**, 341–349.

53 F. Gándara, H. Furukawa, S. Lee and O. M. Yaghi, *J. Am. Chem. Soc.*, 2014, **136**, 5271–5274.

54 H. Tian, T. Li, T. Zhang and X. Xiao, *Int. J. Coal Geol.*, 2016, **156**, 36–49.

55 T. F. Rexer, M. J. Benham, A. C. Aplin and K. M. Thomas, *Energy Fuels*, 2013, **27**, 3099–3109.

56 X. Tang, N. Ripepi, N. P. Stadie, L. Yu and M. R. Hall, *Fuel*, 2016, **185**, 10–17.

57 D. Lozano-Castelló, J. Alcañiz-Monge, M. A. De La Casa-Lillo, D. Cazorla-Amorós and A. Linares-Solano, *Fuel*, 2002, **81**, 1777–1803.

58 C. M. Simon, J. Kim, D. A. Gomez-Gualdron, J. S. Camp, Y. G. Chung, R. L. Martin, R. Mercado, M. W. Deem, D. Gunter, M. Haranczyk, D. S. Sholl, R. Q. Snurr and B. Smit, *Energy Environ. Sci.*, 2015, **8**, 1190–1199.

59 J. Abdulsalam, J. Mulopo, S. O. Bada and B. Oboirien, *ACS Omega*, 2020, **5**, 32530–32539.

60 M. E. Casco, F. Rey, J. L. Jordá, S. Rudić, F. Fauth, M. Martínez-Escandell, F. Rodríguez-Reinoso, E. V. Ramos-Fernández and J. Silvestre-Albero, *Chem. Sci.*, 2016, **7**, 3658–3666.

61 P. Navarro Quirant, C. Cuadrado-Collados, A. J. Romero-Anaya, J. Silvestre Albero and M. Martinez Escandell, *Ind. Eng. Chem. Res.*, 2020, **59**, 5775–5785.

62 M. E. Casco, M. Martínez-Escandell, K. Kaneko, J. Silvestre-Albero and F. Rodríguez-Reinoso, *Carbon*, 2015, **93**, 11–21.

63 T. Tian, Z. Zeng, D. Vulpe, M. E. Casco, G. Divitini, P. A. Midgley, J. Silvestre-Albero, J. C. Tan, P. Z. Moghadam and D. Fairen-Jimenez, *Nat. Mater.*, 2018, **17**, 174–179.

64 S. Dutta, A. Bhaumik and K. C.-W. Wu, *Energy Environ. Sci.*, 2014, **7**, 3574–3592.

65 S. Ma, D. Sun, J. M. Simmons, C. D. Collier, D. Yuan and H. C. Zhou, *J. Am. Chem. Soc.*, 2008, **130**, 1012–1016.

66 B. M. Connolly, M. Aragones-Anglada, J. Gandara-Loe, N. A. Danaf, D. C. Lamb, J. P. Mehta, D. Vulpe, S. Wuttke, J. Silvestre-Albero, P. Z. Moghadam, A. E. H. Wheatley and D. Fairen-Jimenez, *Nat. Commun.*, 2019, **10**, 2345.

67 D. Alezi, Y. Belmabkhout, M. Suyetin, P. M. Bhatt, Ł. J. Weseliński, V. Solovyeva, K. Adil, I. Spanopoulos, P. N. Trikalitis, A.-H. Emwas and M. Eddaoudi, *J. Am. Chem. Soc.*, 2015, **137**, 13308–13318.

68 Z. Chen, P. Li, R. Anderson, X. Wang, X. Zhang, L. Robison, L. R. Redfern, S. Moribe, T. Islamoglu, D. A. Gómez-Gualdrón, T. Yildirim, J. F. Stoddart and O. K. Farha, *Science*, 2020, **368**, 297–303.

69 E. Masika and R. Mokaya, *Energy Environ. Sci.*, 2014, **7**, 427–434.

70 M. Sevilla, N. Alam and R. Mokaya, *J. Phys. Chem. C*, 2010, **114**, 11314–11319.

This journal is © The Royal Society of Chemistry 2023

J. Mater. Chem. A, 2023, **11**, 6952–6965 | **6965**